Droplet-based microfluidics at the femtolitre scale

Journal:	*Lab on a Chip*
Manuscript ID:	LC-ART-09-2014-001122.R1
Article Type:	Paper
Date Submitted by the Author:	17-Nov-2014
Complete List of Authors:	LEMAN, Marie; ESPCI, MMN; École Supérieure de Physique et de Chimie Industrielles de la Ville de Paris, Abouakil, Faris; École Supérieure de Physique et de Chimie Industrielles de la Ville de Paris, Griffiths, Andrew; École Supérieure de Physique et de Chimie Industrielles de la Ville de Paris, Tabeling, Patrick; École Supérieure de Physique et de Chimie Industrielles de la Ville de Paris, ; ESPCI,

Standard operations of droplet-based microfluidic were miniaturized down to the femtolitre scale. The level of control is maintained despite the three order of magnitude reduction in droplet volume.

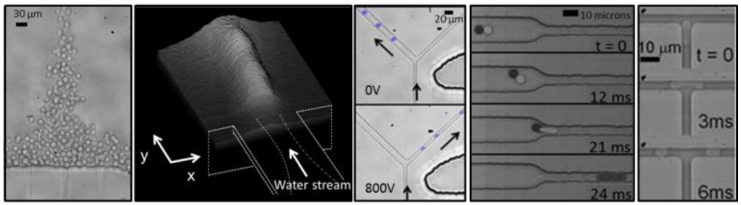

Production Mixing DEP sorting Electrocoalescence Splitting

DROPLET-BASED MICROFLUIDICS AT THE FEMTOLITRE SCALE[†]

Marie LEMAN[a,b], Faris ABOUAKIL[a], Andrew D. GRIFFITHS[b] and Patrick TABELING[a]

[a]Microfluidics, MEMS and Nanostructures Laboratory (MMN), CNRS UMR 7083, École supérieure de physique et de chimie industrielles de la Ville de Paris (ESPCI ParisTech), 10, rue Vauquelin, 75231 Paris Cedex 05, France. Email: patrick.tabeling@espci.fr

[b]Laboratory of Biochemistry (LBC), CNRS UMR 8231, École supérieure de physique et de chimie industrielles de la Ville de Paris (ESPCI ParisTech), 10, rue Vauquelin, 75231 Paris Cedex 05, France. Email: andrew.griffiths@espci.fr

[†]Electronic supplementary information (ESI) available: S1: Mixing inside femtolitre droplets produced by step-emulsification, S2: Mixing inside picolitre droplets produced by step-emulsification, S3: Dielectrophoretic sorting of femtolitre droplets, S4: Electrocoalescence of femtolitre droplets, S5: Splitting of femtolitre droplets, S6: Parallelized production of femtolitre droplets, S7: Reinjection of femtolitre droplets. S8: Fabrication of the molds by multiple-layer soft lithography.

Summary

We have built a toolbox of modules for droplet-based microfluidic operations on femtolitre volume droplets. We have demonstrated monodisperse production, sorting, coalescence, splitting, mixing, off-chip incubation and re-injection at high frequencies (up to 3kHz). We describe the constraints and limitations under which satisfactory performances are obtained, and discuss the physics that controls each operation. For some operations, such as internal mixing, we obtained outstanding performances: for instance, in 75 fL droplets the mixing time was 45 µs, 35-fold faster than previously reported for a droplet microreactor. In practice, in all cases, a level of control comparable to nanolitre or picolitre droplet manipulation was obtained despite the 3 to 6 order of magnitude reduction in droplet volume. Remarkably, all the operations were performed using devices made using standard soft-lithography techniques and PDMS rapid prototyping. We show that femtolitre droplets can be used as microreactors for molecular biology with volumes one billion times smaller than conventional microtitre plate wells: in particular, the Polymerase Chain Reaction (PCR) was shown to work efficiently in 20 fL droplets.

Introduction

By using droplets as microreactors, droplet-based microfluidics[1-8] has allowed biological and chemical systems to be analyzed with high throughputs, small sample volumes, low costs, fast mixing[9], and “digital” analysis of single compartmentalized molecules[10-14] or cells[15,16]. In the state-of-the-art, droplet volumes usually range from 2 pL to 4 nL (15 and 200 µm diameter), one thousand to one million times smaller than microtitre plate wells. Highly monodisperse droplets can be made and manipulated at kHz frequencies: a range of on-chip droplet manipulations such as mixing[9,17,18], splitting[19,20], fusing[21-25], injecting[26], incubating[27-29] and sorting[30-32] have been developed, that can be combined with off-chip incubations followed by re-injection[16]. These operations allow a wide range of processes and assays, some of which require complex, multi-step operations to be implemented in droplet-based microfluidic systems (see, for example[33,34]). This miniaturized technology has developed into a powerful tool for a number of applications[1,4,5,7] including synthesis of small molecules or particles[17,35,36], screening of small molecule libraries[37], screening of antibodies[38,39], screening and directed evolution of enzymes[40-42], targeted sequencing[43] and digital PCR[10-13,44]. Today, droplet-based microfluidic systems for targeted sequencing, next-generation sequencing and digital PCR are commercially available.

Further miniaturizing the droplets down to the femtolitre scale affords significant gains in terms of reduction in reagent consumption and cost, increased throughput, faster thermal transfer and higher mixing speeds. Moreover, there exist areas where use of very small droplets is either advantageous or essential. For example, drug delivery[45] (in which droplets must have volumes < 65 fL to avoid embolism), or “digital biology” approaches based on analyzing single-cells or single-molecules, such as measurement of the activity of single enzyme molecules[14,46,47]. Last but not least, having the capability to generate droplets of colloidal size using microfluidics may open up interesting new avenues in the fields of diagnostics and colloidal materials[48].

The first devices for producing femtolitre droplets at high throughput were demonstrated by Kobayashi[49]. Femtolitre droplets were produced using a step emulsification geometry, with kHz production rates and monodispersivities in the range of a few percent. Using a similar geometry, Malloggi *et al.*[50] extended this approach by demonstrating that complex droplets, such as Janus droplets, double emulsions, UV cured particles, and elementary clusters with volumes in the femtolitre range could be produced. More recently, novel methods of production/parallelization have been proposed[51], enabling MHz production of femtolitre droplets[14].

However, subsequent downstream manipulation of femtolitre droplets has so far been restricted to optical manipulation of individual droplet[52,53]. From a physical standpoint, high-throughput manipulation of femtolitre droplets is challenging due to unfavorable scaling of many operations. By reducing droplet volumes from the pL to fL scale, one considerably affects the balance of forces that governs the physics of the system. For example, picolitre droplets are traditionally sorted using dielectrophoresis[30,31]. By reducing droplet volume by a factor of 1,000, dielectrophoretic forces[54] are reduced by three orders of magnitude while drag forces are decreased by one order of magnitude only. It is thus questionable whether dielectrophoretic forces can overcome drag forces to allow high-throughput dielectrophoretic sorting of fL droplets. Likewise, the destabilization and coalescence of pairs of droplets by an electric field[55] is disfavored by miniaturization as the capillary recovering force (linear in R) decreases more slowly than the competing electrostatic force (square dependence in R). Scaling difficulties are also encountered for droplet splitting[19,20] or droplet coalescence by hydrodynamic forcing[56], as droplets must be confined, which poses problems when using standard microfabrication methods. Last but not least, the surface/volume (S/V) ratio increases on reducing droplet size ($S/V=3/R$). Thus adsorption of reagents to surfaces risks to compromise chemical and biological reactions such as DNA amplification in fL droplets or other highly miniaturized systems[57].

Here we demonstrate that, even though scaling laws look at first sight unfavorable in a number of cases, all the key operations of droplet-based microfluidics can be performed in a highly controlled manner with droplets of a few femtolitres in volume, at kHz rates. We have built up a modular femtolitre droplet toolbox of unit operations: high throughput monodisperse production, sorting, coalescence, splitting, mixing and production, off-chip incubation and re-injection. In certain cases (such as internal mixing), we obtain outstanding microfluidic performances, interesting in their own right.

Experimental section

Device fabrication

Microfluidic chips were fabricated using a classical soft lithography process[58,59]. Silica molds were fabricated with SU-8 negative photoresist (Micro Chem). In most cases, two-layer lithography was used: the silica wafer was first dehydrated at 200°C, then the thin layer (900 nm to 3.6 µm depending on the design) was spin-coated, exposed, and developed. In order to prevent adhesion issues, the post bake time was extremely long (9 minutes) and a hard bake was performed before starting the second layer fabrication. To obtain a thick second layer without an intermediate step, pieces of tape (3M, Magic Scotch) were added onto the alignment structures before the second layer spin-coating. Alignment structures were then fully visible whatever the thickness of the second layer and optical aberrations were suppressed during the alignment procedure. The alignment process was thus very fast and accurate, and a typical ratio between the heights of the two layers of 35:1 was obtained without an intermediate step. The detailed protocol for fabrication of the molds is provided as Electronic Supplementary Information. Poly-(dimethylsiloxane) (PDMS, Sylgard 184, Dow Corning) mixed with 10% (w/w) curing agent was poured over the mold to a depth of 4 mm and incubated at 65°C for around 12 hours. The PDMS was peeled off the mold and the input and output ports were punched with a 0.5 mm-diameter Harris Uni-Core biopsy punch (Electron Microscopy Sciences). 150 µm thick glass slides were spin-coated with a 50 µm PDMS layer and cured. Devices were bonded to these slides with a PDC-002 oxygen plasma cleaner (Harrick Plasma). To obtain hydrophobic systems, bonded devices were then aged at 90°C overnight to enable the PDMS to go back to its native hydrophobic state. Sometimes, the aging was accelerated by heating to 115°C. For thin structures with aspect ratios higher than 10, hard PDMS was sometimes used, with a standard protocol[60].

Apparatus

Unless mentioned, fluids were injected using an MFCS pressure controller (Fluigent) which can apply up to 7 bars. Usual working pressures were 1.5 to 4 bars. For applications where an electrical field was needed, channels were added in the lithographic process and filled with a conductive buffer (Na Cl, 189 g/L, σ = 41 S/m)[61,62]. Electric voltages were produced by an AM300 generator (R&S) and amplified by a BOP1000M amplifier (KEPCO) with a gain of 100. The electric field was applied to the microfluidic device by an Electrowell (Fluigent) through Pt electrodes (Ø 300 µm) plunged into the conductive buffer. Experiments were observed using an inverted microscope (Zeiss, Observer A1), with a 40x or 100x, objective and recorded with a high-speed camera (Photron; Fastcam SA3). For fluorescence measurement, fluorescein was excited with an HBO 100 mercury vapor lamp (Zeiss) through an FITC filter (490 nm)

Formulation

Emulsions were formed using an aqueous phase and fluorinated oil (Novec HFE 7500) containing a non-ionic tri-block copolymer surfactant[63] with two perfluoropolyether (PFPE) tails ($M_W \sim 6000\,\mathrm{g mol^{-1}}$) and a polyethylene glycol (PEG) head group ($M_W \sim 600\,\mathrm{g mol^{-1}}$) at a concentration of 2% (w/w) as the carrier fluid. The interfacial tension between the Novec HFE 7500 oil containing 2% surfactant and DI water with 1% F68 pluronic was 5 mN/m, measured by the pendant drop method using a DSA 30 (Krüss GmbH). Experiments involving fluorescence were carried out with Fluorescein sodium salt, whose dianionic form is highly fluorescent (quantum yield of 0.93) and whose bi-protonated form is non-fluorescent (pKa_1 = 6.4, quantum yield of 0.37, pKa_2 = 4.3, non fluorescent). Conductimetry measurements were carried out with a CDM 210 (Radiometer Analytical S.A.).

Polymerase chain reaction (PCR)

PCR was performed on a 2660 bp pUC18 plasmid, out of which a 129 bp PCR product was amplified with M13 Forward and Reverse primers. The PCR mix consisted of DreamTaq Green Buffer (Thermoscientific, 5 µL/50 µL), M13 Forward and Reverse primers (Thermoscientific, 0.4 µM), dNTPs (Thermoscientific, 200 µM), DreamTaq polymerase (Thermoscientific, 1 µL/50 µL), F68 pluronic (0.02%) and drosophila total RNA (340 pg/µL). DNA concentration was varied from 10 pg/µL to 200 pg/µL. 25 to 65 fL droplets containing the above mix were produced by step emulsification[50]. The droplets were collected in a 200 µL Eppendorf tube and covered with heavy mineral oil to avoid evaporation. PCR was performed in a thermocycler (MJ Research PTC-200) off-chip. The amplification program comprised the following steps; initial denaturation at 94°C for 2 minutes, 35 cycles consisting of DNA denaturation at 94°C for 15 s, primer annealing at 62°C for 30s, extension at 72°C for 30 s, and final elongation at 72°C for 5 min. After thermocycling, the emulsion was broken by adding 30 to 60 µL of perfluorooctanol (approximately three to six times the emulsion volume), and analyzed by electrophoresis on 2% agarose gels in 0.5X TBE buffer containing 0.05 µL/mL of ethidium bromide.

Image analysis

Image analyses were performed using Image J (NIH). To estimate droplet sizes images were thresholded, skeletonized and the analyze particle function used to provide quantitative information on the droplet area and position. Size distributions were also determined in the same way.

To estimate the fraction of coalescence events in a packed emulsion, we identified coalesced droplets by their size and measured the total area of coalesced droplets a_c, the total area occupied by uncoalesced droplets a_u and the total number of uncoalesced droplets n_u. The fraction of coalesced droplets is $C = (a_c/a_u n_u)/(n_u + a_c/a_u n_u)$.

For fluorescence experiments, the IntDen function was used. It allows the product of the mean gray value times the droplet area to be computed. In some cases, image averaging was carried out to enhance the signal to noise ratio.

Results and discussion

Mixing inside droplets

Droplets function as individual reactors of small volume in which dispersion of the reagents is suppressed by the presence of the droplet interface. Thanks to a number of favorable mechanisms (internal recirculations, chaotic regimes), mixing times down to 2 ms have been achieved in µL to pL droplets[9,17]. Here we asked whether, by reducing droplet sizes to femtolitre volumes, faster internal mixing can be obtained.

To investigate this question, we used the diffusion-limited acid base reaction between fluorescein (50 mM) at pH 4 and a basic buffer at pH 9 (30 mM Tris-Base), which is much faster than the mixing times considered hereafter. Protonated fluorescein has a very low fluorescence, while its dianionic form is highly fluorescent. An intercalating stream of acid buffer (10 mM Tris-HCl pH 4) separated the two reagents to prevent prior contact. The three laminar streams flowed side by side (Fig. 1a) and were pinched between two streams of fluorinated oil containing fluorosurfactant.

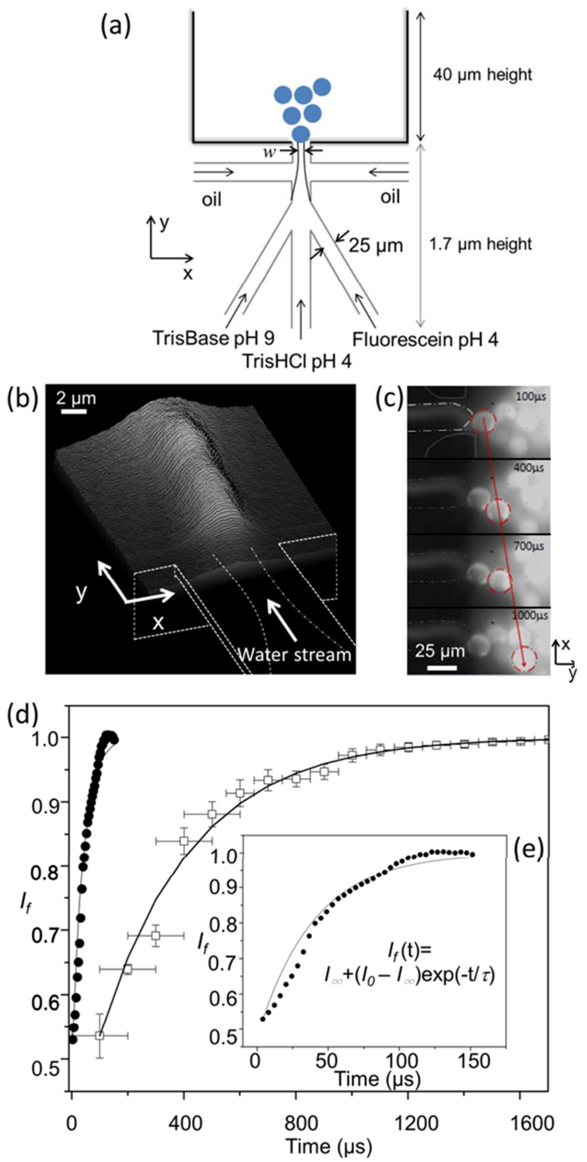

Figure 1. (a) Droplet production and mixing in the step emulsification regime. The increase in fluorescence resulting from fluorescein deprotonation was used to determine the mixing time. Dimensions are indicated for the fL experiments. (b) Surface profile of 75 fL droplet production, with an exposure time of 500 ms. At the step, the fluorescence emission was low then increased along the streamwise direction (y axis). A movie of droplet production can be found in the Supplementary Material (Movie S1). (c) Example of 1 pL droplet production. The location of a selected droplet in successive images is indicated by a red circle. A movie of droplet production can be found in the Supplementary Material (Movie S2). (d) pL droplet fluorescence

was measured using Image J, integrating the fluorescence over the entire drop. The fluorescence intensity $I_f(t)$ (□) was renormalized and averaged over 8 droplets, then fitted to an exponential evolution to obtain the characteristic time, τ_{pico} = 330 µs. The fluorescence intensity extracted from surface profiles of 75 fL droplets production is plotted on the same graph (•). (e) Average fluorescence intensity I_f of 75 fL droplets was determined as a function of the distance to the step and the time-position equivalence was used to determine the time. The fluorescence intensity was renormalized and fitted to an exponential evolution $I_f(t) = I_\infty + (I_0 - I_\infty)\,exp(-t/\tau)$ with Matlab to obtain the characteristic time, τ_{femto} = 45 µs.

Owing to the shallow geometry (1.7 µm height, 25 µm width), no droplets were formed at this stage. On reaching the step, where the channel increased to 40 µm in height and broadened to 100 µm in width, droplet precursors began to form at the step and grew until droplets were generated[64]. Droplets of 75 fL (5.2 µm diameter) were produced at a frequency of 10.7 kHz in the step-emulsification regime. The increase of fluorescence intensity I_f was monitored during droplet production and time-position equivalence was used to replace the position coordinate by time.

Low fluorescence emission and high speeds did not allow femtolitre droplets to be tracked individually in real time. We thus exploited image averaging to enhance the signal to noise ratio to obtain profiles like the one depicted in Fig. 1b, in which space has been converted to time by using the relation $t=y/U$ (with U the aqueous phase speed). Additional experiments carried out with 1.1 picolitre droplets (13 µm diameter) produced at a lower frequency (2.8 kHz) using a step emulsification regime (Fig. 1c) enlightened the hydrodynamics of mixing. In this case, individual droplets could be imaged and tracked after their production and the increase in fluorescence measured by image analysis.

Before the step, the contact time $\tau_{contact}$ between the fluids was short enough to exclude the possibility of diffusive mixing as the fluids flow side by side. The contact time was 3 to 500 times smaller than the characteristic diffusion time τ_{diff} for H^+ and OH^- ions in water, calculated over the width w of the water stream (Fig. 1a). At infinite dilution, $D_{H+} = 9.31.10^{-5}$ cm^2/s, $D_{OH-} = 5.30.10^{-5}$ cm^2/s[65]. For the 75 fL droplets: w = 3 µm, τ_{diff} = 480 µs, $\tau_{contact}$ = 160 µs. For the 1.1 pL droplets: w = 18 µm, τ_{diff} = 17 ms, $\tau_{contact}$ = 60 µs. Calculated diffusion times are overestimated as diffusion coefficients are smaller at finite dilution.

Fig. 1d depicts the renormalized fluorescence measurements in the femtolitre case (•) and in the picolitre case (□). Owing to the different time scales, the femtolitre fluorescence intensity measurement is replotted in Fig. 1e. Experimental data was fitted to an exponential evolution with Matlab (lines in Fig.1d and 1e). Corresponding mixing times are 330 µs in 1.1 pL droplets and 45 µs in 75 fL droplets. The latter result is the shortest time reported to date for a droplet microreactor, 35-fold smaller than fastest time previously reported (2 ms)[18]. We thus demonstrate that miniaturizing droplets to the femtolitre scale allows unprecedented fast mixing times (45 µs).

Dielectrophoretic (DEP) droplet sorting

When driven towards a junction containing two paths of unequal hydrodynamic resistance, droplets (or cells, or particles) choose the hydrodynamic path of least resistance (Fig. 2a). However, when subjected to a non-uniform electric field, droplets become electrically polarized and a dielectrophoretic (DEP) force can drive the droplets into the channel of highest resistance[30]. This is how active sorting of droplets is classically achieved. However, DEP forces are expected to decrease with the volume of the droplet[54], and we may wonder whether miniaturization will jeopardize DEP sorting.

In our experiments, droplets are sent towards a Y junction (Fig. 2a), and completely obstruct the channel prior to the bifurcation. In such conditions, the pressure drop across a plug is given by[66]:

$$\Delta P = R_h l u \sim \frac{\eta}{wh}\, lu \qquad (1)$$

Where R_h is the fluidic resistivity, u the droplet speed (close to the flow speed U_c at low capillary numbers[66]), η the droplet viscosity, w the width of the channel, h its height, and l the plug length. The resulting force F_h that drives the plug downstream is thus given by:

$$F_h = \Delta P * S \sim \eta l u \qquad (2)$$

in which $S \sim wh$ is the droplet area (projected normally to the mean flow) on which the pressure field applies. When the obstructing droplet arrives at the junction, if the difference between the hydrodynamic resistances of the two paths is large, the droplet will be driven into the least resistive branch with, in terms of order of magnitude, the same force F_h. In the presence of a non-uniform electric field, the droplet will be attracted towards the more resistive channel by DEP forces. In order to achieve sorting, these forces must overcome F_h. The DEP force is proportional to the volume of the droplet whl and to the product the electric field times its gradient[54]:

$$F_{DEP} \sim \varepsilon_0 \varepsilon_c whlE.\nabla E \qquad (3)$$

where ε_0 is the vacuum permittivity, ε_c is the permittivity of the carrier fluid. The critical electric field E that must be applied to overcome the hydrodynamic drag is thus given by the expression:

$$\eta l u \sim \varepsilon_0 \varepsilon_c whlE.\nabla E \qquad (4)$$

Equation (4) implies the existence of a threshold speed, $u_{thresh}(E)$, above which sorting cannot be achieved:

$$u_{thresh}(E) = \alpha \frac{1}{\eta} \varepsilon_0 \varepsilon_c whE.\nabla E \qquad (5)$$

Where α is a numerical prefactor determined empirically. In practice, the maximum electric field E_{max} that can be applied is limited by electrosplitting[67]:

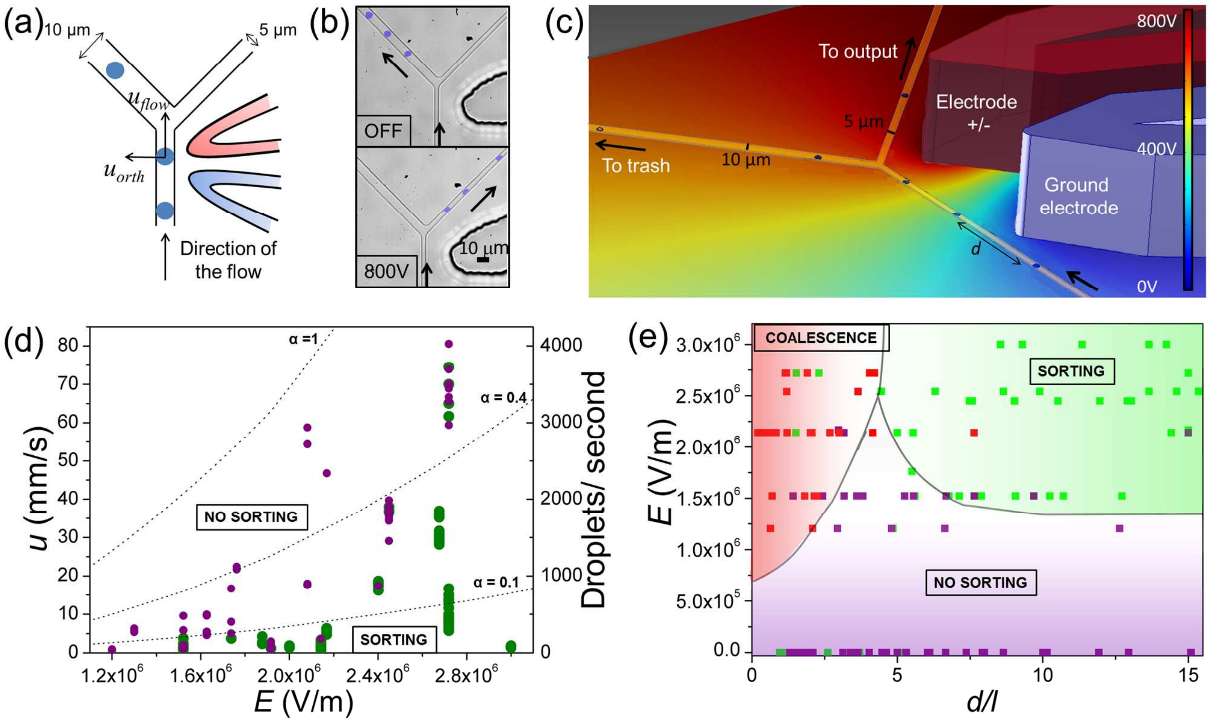

Figure 2. DEP sorting. (a) Droplets are driven towards a y-shaped junction comprising two channels of unequal hydrodynamic resistance. (b) In the absence of an electric field all the droplets pass into the wider channel. Application of an electric field gradient steers droplets by DEP into the narrower channel. A movie of droplet sorting can be found in the Supplementary Material (Movie S3).(c) Perspective representation of the sorting area. COMSOL calculated electric potentials are indicated. (d) Speed of isolated droplets vs the applied electric field. Green dots: droplets directed towards the narrow channel. Purple dots: droplets directed towards the wide channel. The dotted line represents the theoretical maximum speed that enables DEP actuation calculated using Equation (5), with α = 0.1, 0.4 and 1. The corresponding number of droplets per second are calculated assuming a distance of 5*l* between 20 fL consecutive droplets. (e) Phase diagram of the femtolitre DEP sorter. Green: sorted, purple: unsorted, red: undesired coalescence events. The DEP force becomes strong enough to direct droplets at applied fields larger than 1.5.10^6 V/m. Droplets speed were limited to 0,6 – 9 mm/s. Under a critical distance *d/l* = 5, droplets coalesce in this device.

$$E_{max} \sim \sqrt{\frac{\gamma}{\varepsilon_0 \varepsilon_c w}} \quad (6)$$

where γ is the surface tension. As $\nabla E \sim E/\delta$, where δ is the distance between the electrodes, combining (5) and (6), one obtains a critical droplet speed $u*$ above which no sorting can be achieved:

$$u^{*} \sim \frac{\alpha h \gamma}{\eta \delta} \quad (7)$$

Assuming further that the minimal distance d_{min} between consecutive droplets is in the order of a few droplet lengths l, one obtains the maximum droplet sorting frequency f_{max}, from the following relation:

$$f_{max} = \frac{u^{*}}{d_{min}} \sim \frac{\alpha h \gamma}{l \eta \delta} \quad (8)$$

This formula shows that miniaturization should favor higher sorting frequencies, since h, l and δ scale down with the same factor, implying that f_{max} is inversely proportional to the device characteristic dimension.

In our experiments, embedded electrodes were added next to the Y junction during the lithographic process; this guaranteed that the electrodes were aligned with the microfluidic channel with micrometric precision, and they were close enough to generate large electric field gradients (Fig. 2a). The applied AC electric fields were generated by applying between 400 and 1000 V through Pt electrodes plunged in the conductive buffer, at a frequency of 1.5 kHz. Modeling of the electric field distribution was obtained through a finite element analysis with COMSOL multi-physics, considering the 3D system and the electrical parameters of the PDMS and the fluids involved (Fig. 2c). Local fields at the junction were found to vary from 1.1.10^6 to 3.10^6 V/m and are close to the theoretical limit E_{max} for femtolitre droplet splitting (3.1.10^{6}V/m for 40 fL droplets)[67]. Such fields would not be admissible for picolitre droplets, because that they are above the critical field producing droplet breakup at rest (E_{max}= 1.2.10^{6}V/m for 15 pL (30 µm diameter) droplets).

Droplets of 20 to 50 fL volume containing deionized water with 1% pluronic were produced on-chip with a step-emulsification process and driven towards a Y-shaped junction, with a hydrodynamic resistance ratio κ = 1.6 between the two paths. With κ = 1.6, the wide channel can contain up to 14 circulating droplets without substantially perturbing the main channel resistance[68]. The sorter was tested with trains of droplets travelling at velocities, u, ranging from 0.6 to 90 mm/s, varying the applied voltage V and the spacing d between the droplets. This corresponds to 8 to 9000 droplets/s, depending on u and d. Image processing was used to determine the droplet length l parallel with the flow, the distance d to the preceding droplet and the droplet trajectory.

In the absence of an electric field, all droplets passed into the low resistance channel, but by applying a voltage to the electrodes, it was possible to direct the stream of droplets into the high resistance channel (Fig. 2b). As predicted by the above theory, DEP sorting was possible only below a threshold velocity. Fig. 2d shows that well spaced droplets ($d/l \geq 15$) were correctly driven towards the narrow channel at low speeds (green dots), but they flow into the large channel in the presence of an electric field above a critical speed $u_{thresh}(E)$ (purple dots). Experimentally, below $E = 1.5.10^6$ V/m, no speeds were found to enable DEP actuation, implying the threshold speed is lower than 0.6 mm/s in such conditions. The dotted lines represent the theoretical threshold speed, calculated using Equation (5) and electric field gradients computed with COMSOL, for $\alpha = 0.1$, 0.4 and 1. One sees that $\alpha = 0.1$ describes correctly the experimental trend at low electric fields, but $\alpha = 0.4$ better matches the experimental data at high fields. The discrepancy between theory and experiment most likely comes from the simplicity of our model; at high electric fields, droplets tend to deform, a parameter discarded from the discussion. A more accurate assessment would need to take into account the detailed shape of the droplet, its dynamical evolution during the sorting process, but also the presence of surfactants and the precise flow geometry at the junction, which is beyond the scope of this paper.

Fig. 2e shows an overview of the regimes of sorting found for various applied electric fields and distances between consecutive droplets, d (expressed as the ratio d/l) with u = 0.6 – 9 mm/s. Three regimes were observed, which are color-coded in Fig. 2d: droplets passing into the wide channel (purple), droplets passing into the narrow channel (green), and droplets electrocoalescing (red). In the absence of an electric field (0V), with $d/l > 5$, all 716 analyzed droplets passed into the wide channel. In the presence of a low electric field, in agreement with the study of well spaced droplets (Fig. 2d), no droplets were correctly sorted. Above $E = 1.5.10^6$ V/m, sorting was possible. In such conditions, droplets were correctly sorted as long as they were not perturbed by the preceding droplet. Fig. 2e indicates that the distance between consecutive droplets has to be above $d/l \approx 5 - 6$ to enable efficient sorting, without sorting errors or coalescence events caused by the proximity of the preceding droplet. The maximum sorting frequency obtained experimentally was 3 kHz for 20 fL droplets, which is an improvement compared to maximum sorting rates observed for picolitre droplets (2 kHz)[31,41]. To assess the theoretical maximum frequency at the electrosplitting limit, we assumed α was close to 0.4, and assessed the term $E.\nabla E$ in COMSOL at the theoretical limit $E_{max} = 3.5.10^6$ V/m for 20 fL droplet splitting. Equation (5) then gives $u_{thresh}(E_{max}) = 203$ mm/s, and $f_{max} = 8$ kHz. It may be possible, therefore, to further improve the sorting speed by increasing the applied electric field.

To summarize, we have shown that sorting of streams of femtolitre droplets under high throughput conditions is feasible. This operation is achieved by increasing the electric field, which is possible owing to the fact that electrosplitting of droplets is inhibited by miniaturization.

Pairwise electrocoalescence

When subjected to a uniform electric field, water droplets in a dielectric phase get polarized and an attractive force operates between each dipole droplet[69]; as droplets approach, the film that separates them thins out and eventually breaks up, leading to coalescence. Furthermore, each droplet dipole locally increases the electric field as they get closer[69], thus deforming the interfaces and enhancing the coalescence process. The physics that underlies this process can be described by two dimensionless parameters[70,71,55]: i) The Bond electrical number, $B_e = \varepsilon_0 \varepsilon_c E^2 R / \gamma$, represents the ratio of the electrical force that tends to deform the droplets over the restoring capillary force. Here E is the field quadratic mean and R is the droplet radius ; ii) The ratio of the initial distance between droplets over their radius d/R, which is related to the intensity of the interaction between droplet dipoles.

In the literature, it is well established that coalescence occurs at Bond numbers below unity (typically $B_e = 0.2 - 0.5$). This implies that, as droplet radius, R, decreases by a factor of ten, electric fields needed to induce coalescence are increased by a factor of ~3 ($\sqrt{10}$). The question is whether this is feasible.

In the experiments, electrodes were added close to the coalescence zone during the soft lithography process in order to obtain high electric fields. Two sets of 20 to 30 fL aqueous droplets were generated at 3 kHz using an on-chip step emulsification process, and brought together just upstream of the coalescence zone (Fig. 3a). The coalescence zone was designed to favor the pairing of droplets and to assist the electrocoalescence process through decompression of the droplet-pairs at the restriction at the exit of the coalescence chamber[56]. Electrodes were positioned slightly asymmetrically around the channel to ensure that the highest electric field was located at the restriction. To assess the electric field effectively applied in the channel, 3D COMSOL Multiphysics simulations were performed, taking into account the material's electrical characteristics (Fig. 3b).

Droplets entered the coalescence chamber at speeds ranging from 2 to 22 mm/s and the coalescence process was tracked by analysing images taken with a high-speed camera. An example of coalescence of two droplets, containing brilliant black (2%) and fluorescein (1%) is shown in Figure 3c. Phase diagrams were drawn for two solutions of different conductivity: deionised water with F68 pluronic (1%) and deionised water with fluorescein (300 μM) (Fig. 3d). Their conductivities were, respectively, 10^{-3} S/m and 10^{-1} S/m. When subjected to the electric field, droplet free charges

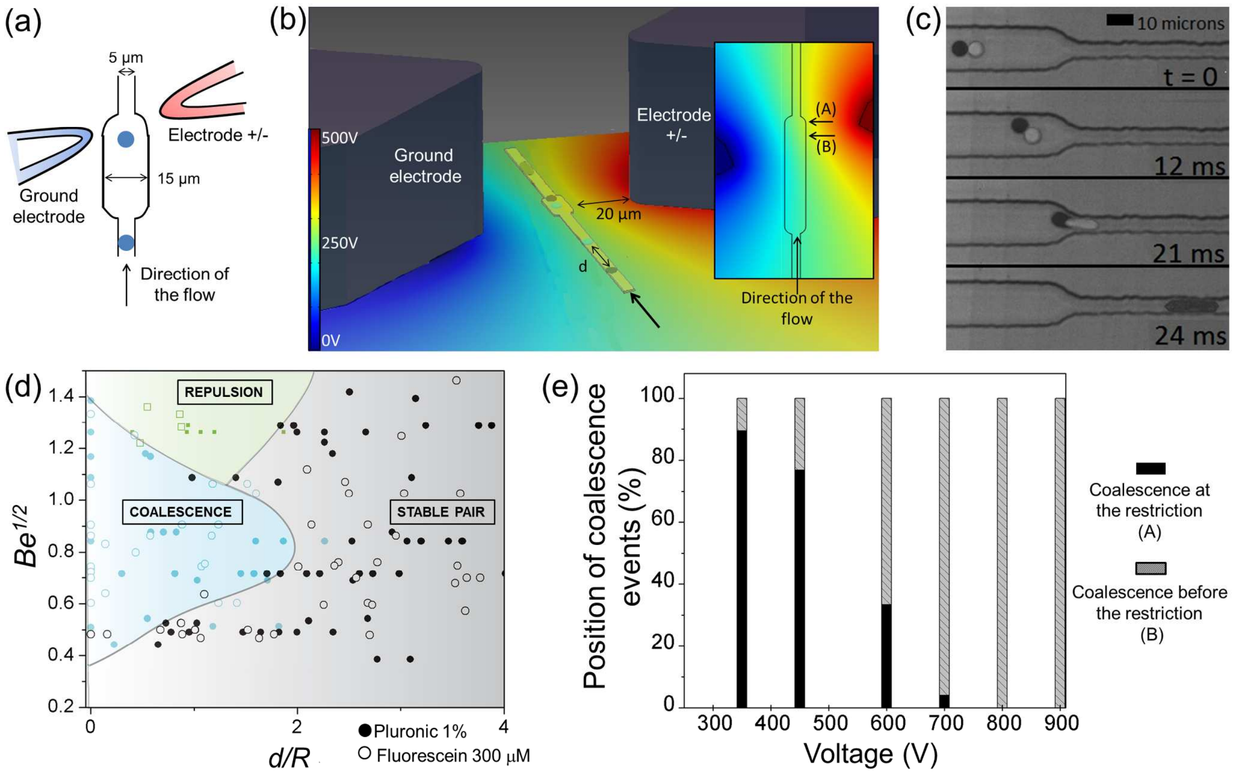

Figure 3. Electrocoalescence. (a) Electrocoalescence device. Droplets of 25 fL volume, generated by two drop makers, were brought together and enter a coalescence zone designed to favor droplet pairing and coalescence. Electrodes were added around this zone to ensure efficient electrocoalescence of the droplet pairs. (b) Perspective representation of the coalescence region, with the electric potential calculated by COMSOL. The inset represent in more details the coalescence area. Electrodes are positioned slightly asymmetrically to ensure that the highest electric field (Position B) is located near the restriction (Position A). (c) Example of a coalescence event for 25 fL droplets colored with Brilliant Black (2%) and Fluorescein (1%), respectively. The applied voltage was 450 V. Droplets reorient along the field (t = 12ms) and then coalesce at the restriction (t = 21ms). The channel height is 1 µm. A movie of droplet coalescence can be found in the Supplementary Material (Movie S4) (d) Phase diagram of the system. Blue area: coalescence. Gray: stable pair. Green: repulsion. Experiments were carried out using droplets containing (o) 300 µM fluorescein and (●)1% Pluronic F68, without observable differences between the two solutions. (e) Percentage of droplets coalescing in position A (black) or position B (gray), as a function of the voltage applied.

move with a time constant $\tau = \varepsilon_0\ \varepsilon_d\ /\ \sigma$, where ε_d is the permittivity of the dispersed phase, ε_0 the vaccum permittivity, and σ the dispersed phase conductivity. This time constant is much smaller than the excitation period in both cases ($\tau = 10^{-7}$ s and 10^{-9} s $<< \tau_{ex} = 0.7$ ms) which guarantees that droplets get polarized instantly and act as charged conductors.

We measured the radius R and the distance between paired droplets, *d,* at the entrance of the coalescence area. The distance between consecutive droplet pairs was maintained above $4R$ to avoid droplet-droplet interactions[55]. Under this condition, the maximum coalescence throughput of the device was 1.1 kHz.

Similarly to picolitre droplets[55], three regimes were observed depending on the field strength and on the initial separation *d* between successive droplets: droplet coalescence (Fig. 3c blue area), stable droplet pairs (Fig. 3c grey area), and repulsion between droplets (Fig. 3c green area)[72,73]. No difference in behavior was observed between the two solutions of different conductivities. The phase diagram (Fig. 3d) has a structure similar to that established for picolitre droplets[55], with a triple point separating the three regimes. However, on analysing in more detail the phase diagram, one sees that droplets coalesce up to an initial separation distance of $2R$, compared to $0.7R$ usually found for picolitre droplets. This is presumably due to the geometry: droplets need to deform to enter the restriction which causes their average speed to be slowed down by 50% just before the restriction. This eases the synchronization of droplets in the coalescence area. The position of coalescence events was highly dependent on the electric field (Fig. 3e). Above 800V, all coalescence events happened before the constriction (Position B), whereas droplets coalesced at the restriction at lower fields (Position A). This can be explained by the fact that the mechanism of coalescence depends on the voltage: at high fields, only electric stresses are at play, whereas at lower voltages, droplet coalescence results from both electric stress and hydrodynamic decompression at the restriction.

To summarize, we demonstrate here that controlled electrocoalescence of femtolitre droplets can be achieved in a microfluidic environment, at the expense of applying larger electric fields than for picolitre droplets. The coalescence chamber design favors droplet pairing at larger initial distance and helps destabilization of the pair at the restriction.

Splitting

When droplets are driven towards a T-junction at high speeds, they may either breakup or flow along one of the arms of the T. Mechanical splitting is controlled by the geometry, the viscosity ratio of the continuous and dispersed phase $\lambda = \mu_c / \mu_d$ and the Capillary number, defined by $Ca = \mu_c u/\gamma$. It has been shown that two regimes of splitting are possible, one in which droplets occupy only a fraction of the channel width (non obstructed regime), and the other in which droplets completely obstruct the channel (break up with complete obstruction of the channel)[21,22]. The former necessitates moderately low Ca, while the latter, being mostly controlled by the geometry, occurs almost independently of Ca[20,74]. Since the capillary numbers for fL droplets are typically small (below 10^{-2}), it is difficult in practice to achieve break up in the non obstructed regime: the underlying reason is that the geometries needed to handle fL droplets result in channels with high hydrodynamic resistance, which limits droplet speeds and typically results in small Capillary numbers.

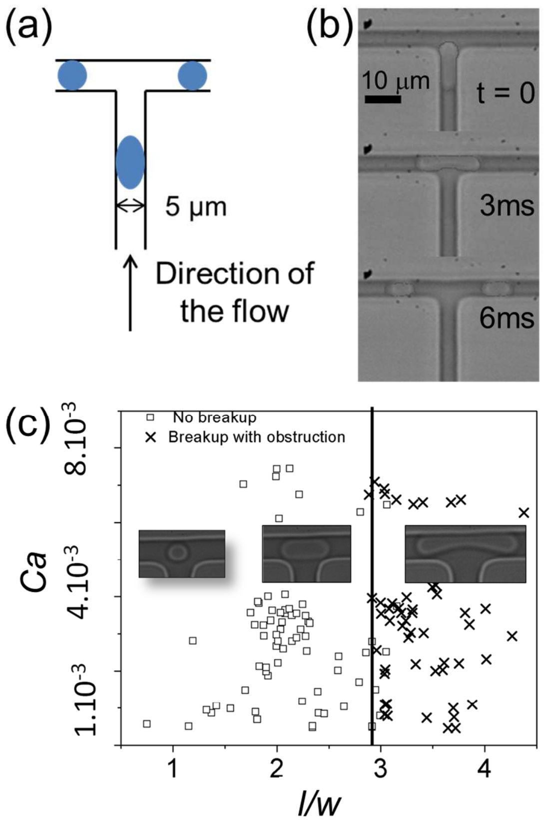

Figure 4. Droplet splitting. (a) Splitting device. Droplets flow towards a T junction. The height of the channel was 1 µm to favor obstruction and enhance the splitting process. (b) Time series of micrographs showing a 75 fL droplet splitting. A movie of droplet splitting can be found in the Supplementary Material (Movie S5) (c) Phase diagram of the splitting of 25 to 135 fL droplets. Only two regimes were observed: (□) non breakup, and (x) breakup with obstruction (at $l/w \geq 3$). This corresponds to a droplet volume of 75 to 130 fL in our geometry, depending on the PDMS pressure related deformation.

In our case, 25 to 135 fL droplets were generated by on-chip step emulsification and driven toward a 1 µm high, 5 µm width T-junction (Fig. 4a). The viscosity ratio between the oil and the water phase is $\lambda = 1.43$. Droplets were driven towards the junction and experiments were recorded by a high-speed camera (Fig. 5b). Droplet speeds and droplet lengths l, were measured by image analysis. The channel width w was also measured *in situ*, so as to take into account the PDMS deformation.

Throughout the experiments, we spanned a range of inlet pressures from 1.5 to 6 bars. Because of the geometry (long thin channels), the corresponding speeds were low - between 5 and 50 mm/s. Attempts to achieve higher flow rates were made with a neMESYS syringe pumps, but the glass slides could not withstand the corresponding applied pressures. To avoid unwanted interactions, the distance between successive droplets was kept above $4l$, limiting the frequency to 850 Hz at the maximum speed of 50 mm/s.

As expected from the low Capillary number of the system, breakup was only observed in the complete obstruction regime. Figure 4c shows that the critical ratio l/w upon which breakup is obtained does not depend on the Capillary number, consistent with theory, but is mostly controlled by the geometry. According to the model described in[74], the breakup with tunnels regime could only be achieved at capillary numbers of 10^{-2}, a range that is difficult to achieve in our device.

To summarize, we demonstrate here that femtolitre droplets splitting is achievable in T junctions in obstructed regimes, with a minimal volume of 75 fL (daughter droplets of 32 fL each) and a maximum frequency of 850 Hz. To split smaller droplets would require either smaller features, beyond the scope of standard soft-lithography techniques, or higher Capillary numbers, thereby higher pressures, which were out of reach with our device.

Droplet stability

The question we address here concerns the thermodynamic stability of femtolitre droplets, stability being a pre-requisite if such droplets are to be used as microreactors for chemical or biological reactions. According to the Epstein-Plesset dissolution model, established for gas bubbles in a liquid solution[75] and later extended to liquid microdroplets dissolution[76], the miniaturization increases the shrinking rate of droplets, by driving faster mass exchanges between them and the continuous phase. On the other hand, the process is known to be inhibited by the addition of solutes[77-79]. In these papers, the solutes are assumed to be insoluble in the continuous phase. Let us denote the subscripts α for the droplet and β for the surrounding phase, 1 for water, 2 for oil and 3 for the solutes. The oil reservoir is assumed to be infinite. At equilibrium, water chemical potentials in the droplet and in the surrounding phase are equal:

$$\mu_{1,\alpha}(T, P_\alpha) = \mu_{1,\beta}(T, P_\beta) \qquad (9)$$

The equilibrium is stable under the condition[77]:

$$\left[\frac{\partial\left(\mu_{1,\alpha}(T,P_\alpha)-\mu_{1,\beta}(T,P_\beta)\right)}{\partial R}\right]_{eq} > 0 \quad (10)$$

On the other hand, there is a relation between the fraction of water in the dispersed phase $x_{1,\alpha}$, the continuous phase $x_{1,\beta}$, and the laplacian pressure term across the droplet interface[72]:

$$v_{m1}\,\frac{2\gamma}{R_{eq}} + RT\ln(x_{1,\alpha}) = RT\ln(x_{1,\beta}) \quad (11)$$

Where v_{m1} is the molar volume of water and R_{eq} is the radius of the droplet at equilibrium.

Inside the droplet, $x_{1,\alpha} = 1 - x_{3,\alpha}$, where $x_{3,\alpha}$ is the fraction of solutes in the droplet at equilibrium; ln(1-$x_{3,\alpha}$) can be developed at first order in the vicinity $x_{3,\alpha} \ll 1$. The fraction of solutes in the droplet at equilibrium $x_{3,\alpha}$ is increased by a factor $(R_0 / R_{eq})^3$ as droplets shrink:

$$v_{m1}\,\frac{2\gamma}{RT\,R_{eq}} - x_{3,\alpha,0}\left({}^{R_0}\!/_{R_{eq}}\right)^3 = \ln(x_{1,\beta}) \quad (12)$$

where R_0 is the initial droplet radius and $x_{3,\alpha,0}$ is the initial fraction of solutes in the droplet. The application of condition (10) to equation (12) gives the minimal fraction of solutes $x_{3,\alpha,0}{}^*$, and hence the minimal concentration of solutes $c_{3,\alpha,0}{}^*$, under which droplets are stable:

$$x_{3,\alpha,0} > x_{3,\alpha,0}{}^* = \frac{2\gamma v_{m1}}{3RTR_0} \quad (13)$$

$$c_{3,\alpha,0} > c_{3,\alpha,0}{}^* = \frac{2\gamma v_{m1}\rho_1}{3RTR_0M_{solute}} \quad (14)$$

Where $\rho_1$is the volumic mass of water and M_{solute} is the molar mass of the solute. With droplet miniaturization, higher solute concentrations are needed to obtain stable droplets. For a typical $M_{solute} =$ 300 g/mol, the minimum solute concentration as a function of droplet volume is presented in Table 1. Despite the increase in $c_{3,\alpha,0}{}^*$ on miniaturization, the values remain accessible experimentally, and femtolitre emulsions can easily be stabilized with proper formulation. We recall that the theory corresponds to an infinite reservoir of the continuous phase. However, in reality, the emulsion reservoir is finite, and shrinkage is expected to stop once the continuous phase is saturated with water and the chemical potentials in the droplet and in the surrounding phase are equal. In this case, the minimum initial solute concentrations required for stability, will be lower than those in Table 1.

Droplet volume	4 fL	60 fL	500 fL	5pL
Minimum solute concentration $c_{3,\alpha,0}{}^*$	80 µM	28 µM	14 µM	6 µM

Table 1. Minimum initial solute concentration $c_{3,\alpha,0}{}^*$ to obtain stable droplets, for several values of droplet volume, and $M_{solute} =$ 300 g/mol.

In our experiments, droplets of 65 fL volume were produced using a parallelized step-emulsification device (Fig. 5a-b). The aqueous phase flows through an array of 37 narrow channels (1 µm high, 5 µm wide), and falls into a deep reservoir of oil (35 µm deep), giving a total droplet production frequency of ~10 kHz. When composed of DI water ($c_{3,\alpha,0} =$ 0), droplets disappeared in a few seconds (Figure 5c, ○) in agreement with the theory. Droplets containing high solute concentration (for instance, PCR reagents, with $c_{3,\alpha,0}$ over ~ 2 mM) demonstrated a better stability. To go deeper, we measured the droplet size distribution by injecting an emulsion comprising 65 fL droplets containing PCR reagents between two glass slides and carried out image analysis (Fig. 5c-d). Just after their production, droplets shrunk slightly towards their radius of equilibrium (0.1 days). Then, the mean radius remained constant over 5 days, before increasing towards higher radii (12 days after the production). The variance in radius (Fig. 5d) remained small at short times (up to 2 days) and slightly increased at longer times (12 days).

The slight initial shrinking is most likely caused by the low but non-zero solubility of solutes in oil. In this case, size distribution depends on the diffusion rates of the solutes and is expected to decrease slightly in the case $c_{3,\alpha,0} \gg c_{3,\alpha,0}{}^*$, $c_{3,\beta,0} = 0$[79]. The increase in size distribution observed at long time scales most likely results from coalescence events rather than Ostwald ripening because the average droplet volume increases.

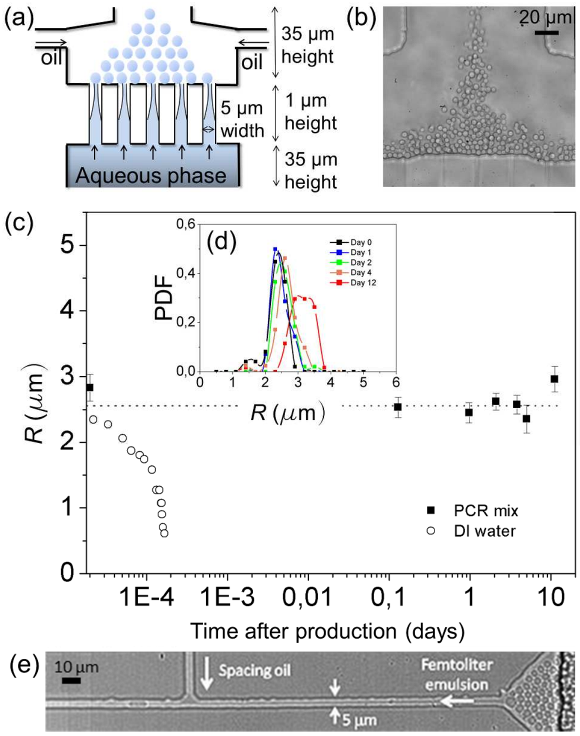

Figure 5. Off-chip droplet incubation and reinjection. (a) Diagram of the parallelized femtolitre droplet maker. (b) Micrograph of a parallelized femtolitre droplet maker. A movie of the production of 65 fL droplets can be found in Supplementary Material (Movie S6). (c) Evolution of the average radius of 65 fL droplets containing DI water (○) or PCR reagents (■) after droplet production and during storage at room temperature under mineral oil. (d) Evolution of the probability

density function (PDF). Black : day 0, dark blue: day 1, green: day 2, orange: day 4, red: day 12. The monodispersity remained high during the first two days (Coefficient of variation (CV) 0.02) and started to decrease after 4 days of incubation at room temperature (CV 0.16 at day 12). (e) Reinjection of a femtolitre emulsion. The channel was 1 µm high, increasing the apparent radius of droplets and enabling one-to-one injection without leaving standard soft lithography processes. A movie of emulsion reinjection can be found in Supplementary Material (Movie S7).

When performing chemical or biological reactions in droplets, many studies focus on performing incubation steps on-chip, but this is associated with a variety of technological issues, notably related to evaporation due to the porosity of PDMS. A way to avoid these issues is to recover the emulsion off-chip, incubate off-chip, and reinject the emulsion into another chip for analysis.

After overnight incubation at room temperature, the 65 fL droplets containing PCR reagents were reinjected and spaced with fluorinated oil with 2% fluorosurfactant. Regular spacing of droplets demands a nozzle as narrow as the droplet diameter, to allow just one droplet to be separated by spacer oil at a time. To obtain such characteristics with 65 fL droplets, the channel height was lowered to 1 µm. The squeezed micrometric droplets have an increased effective radius and could be reinjected in a controlled way in 5 µm width channels accessible by standard soft lithography process with a chrome mask. (Fig. 5e).

To summarize, aqueous femtolitre droplets are thermodynamically stable, provided the aqueous phase contains a low concentration of solute. Under these conditions femtolitre droplets can be incubated for a few days off chip and reinjected on-chip for further analysis. This stability ensures that incubation of biochemical reactions can be performed inside femtolitre droplets, as presented below.

Polymerase chain reaction (PCR) in femtolitre droplets

The Polymerase chain reaction (PCR) is one of the most important biochemical reactions, allowing exponential amplification of target DNA via cycles of enzymatic polymerisation with temperature cycling. However, one can question the impact of droplet miniaturization on the amplification yield, since the surface to volume ratio varies inversely to the droplet radius, and surface effects are expected to become increasingly important.

Droplets of 20 or 65 fL volume containing PCR reagents were produced using the parallelized step-emulsification device described above (Fig. 5a-b). PCR was performed on a 2660 bp pUC18 plasmid, out of which a 129 bp PCR product was amplified with M13 Forward and Reverse primers. Several measures were taken to overcome adsorption issues. The reaction mixture was supplemented with 0.2% F68 Pluronic and *Drosophila* total RNA was added to the DNA dilutions and to the PCR mix at a final concentration of 340 pg/µL. Silanization of the polypropylene reservoirs was also performed, using dimethyldichlorosilane and a classical protocol[80]. The template DNA concentration was varied from 10 pg/µL to 200 pg/µL which corresponds to a mean number of template DNA molecules per 65 fL droplet, λ, ranging from 0.22 to 4.5.

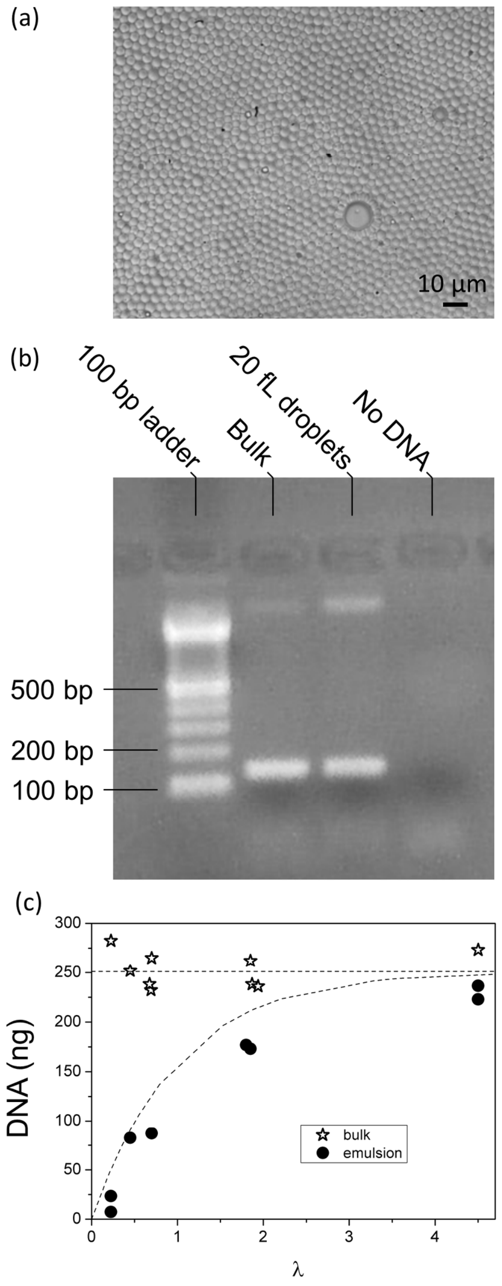

Figure 6. PCR in droplets. (a). Picture of a PCR emulsion after thermocycling. (b) Example of analysis by agarose gel electrophoresis of PCR in 20 fL droplets, mean number of template DNA molecules per droplet λ = 1.85. (c) Final yield of DNA after PCR versus the mean number of template DNA molecules, λ, per 65 fL reaction volume in bulk (stars), and in 65 fL droplets (dots). Dotted lines represent the mean amplification in bulk, and the expected Poisson distribution in emulsion.

After production, droplets were collected in a 200 µL Eppendorf tube and covered with heavy mineral oil to avoid evaporation. PCR was then performed in a thermocycler off-chip. Figure 6a depicts a typical example of the emulsion distribution after thermocycling: the emulsions suffered very few coalescence events during the cycling (0.3%). After thermocycling, the emulsion was broken by adding 30 to 60 µL of perfluorooctanol, and analyzed by agarose gel electrophoresis together with the same reaction performed in bulk (Fig. 6b). Primers were the limiting reagent in this PCR reaction. As a consequence, in bulk the final yield of DNA does not depend upon the initial DNA concentration. (Fig. 6c).

In droplets, however, the final yield of DNA is expected to drop quickly when $\lambda \leq 1$. This is because the template DNA should be distributed into droplets following a Poisson distribution and when $\lambda \leq 1$ an important fraction of droplets does not contain a template DNA molecule (33% at $\lambda = 1$). The final yield of DNA should fit the curve describing the fraction of drops containing ≥1 template DNA molecules $f_o = 1 - e^{-\lambda}$.

The yield of amplified DNA at $\lambda = 4.5$ in femtolitre droplets was similar to in bulk, but dropped off as λ decreased, closely fitting the curve described by a Poisson distribution without loss of template DNA. These results indicate that femtolitre droplets can be used for quantitative biological assays, despite the high surface to volume ratio.

Conclusion

We have built a femtolitre droplet toolbox of basics droplet-based microfluidic operations (Fig. 7). Despite the small size of the droplets, we obtained a level of control comparable to that obtained for nanolitre and picolitre droplets, while still fabricating the chips using standard soft-lithography techniques and rapid PDMS technology. The ability to perform biochemical reactions in femtolitre droplets was checked by performing PCR in the droplets: no loss of reagents was observed and the reaction was equally as efficient as in bulk, despite the high surface to volume ratio. Some operations were more difficult to achieve such as splitting, which is accessible only in the obstructed regime. However, in some other cases miniaturization to femtolitre droplets offered significant advantages. Notably, mixing time was only 45 µs, the shortest reported time in a droplet microreactor. We envisage that the new capabilities to manipulate femtolitre droplets we demonstrate here will inspire the development of novel and innovative systems, able to operate under ultrahigh-throughput conditions using unprecedentedly low volumes of reagents (~one billion times lower than in conventional microtitre-plate based systems).

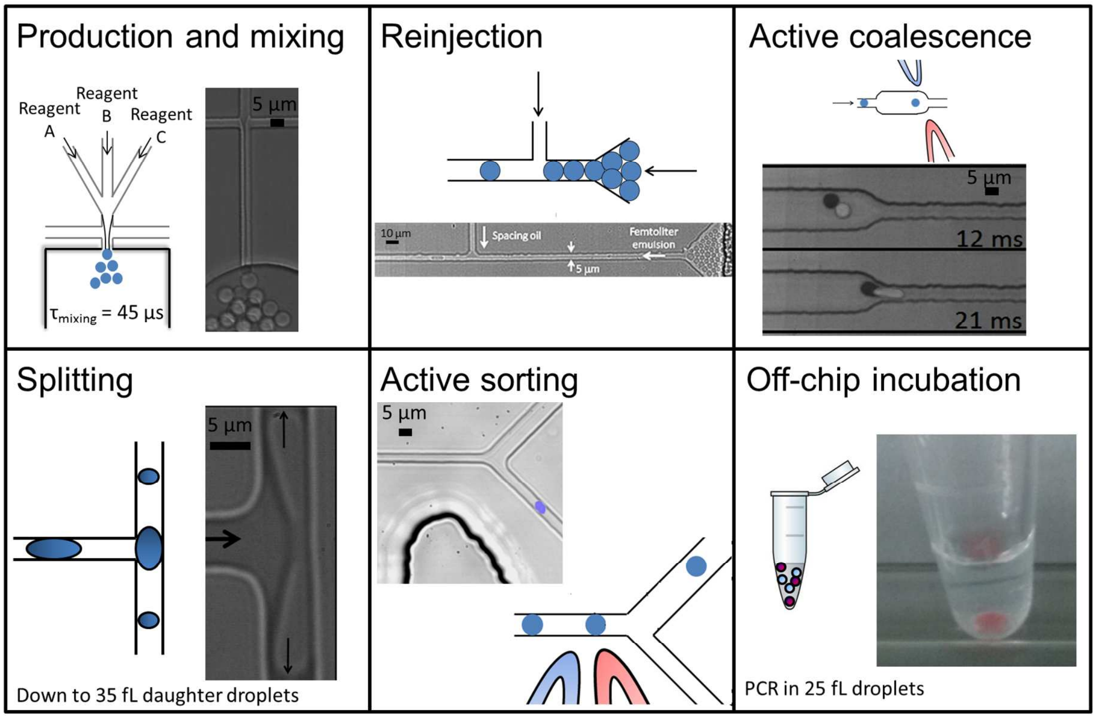

Figure 7. Femtolitre toolbox of unit operations for droplet-based microfluidics.

Acknowledgments

We thank Fabrice Monti for his technical support, Loïc Becerra for the fabrication of chrome masks, Michael Ryckelynck, Hélène Geoffroy, and Matteo Bellucci for fruitful discussions. This work is supported by funding from the French National Research

Agency (ANR) under the "Investissements d'Avenir" program (DigiDiag, reference: ANR-10-NANB-0002-05 and ANR-10-NANB-0002-01).

References

1. S. Y. Teh, R. Lin, L. H. Hung and A. P. Lee, *Lab Chip*, 2008, **8**, 198-220
2. R. Seemann, M. Brinkmann, T. Pfohl and S. Herminghaus, *Rep. Prog. Phys.*, 2012, **75**, 016601.
3. T. P. Lagus and J. F. Edd, *J. Phys. D: Appl. Phys.*, 2013, **46**, 114005.
4. T. Schneider, J. Kreutz and D. T. Chiu, *Anal. Chem. (Washington, DC, U. S.)*, 2013*,* **85**, 3476-3482.
5. S. Vyawahare, A. D. Griffiths and C. A Merten, *Chem. Biol. (Oxford, U. K.*), 2010*,* **17**, 1052-1065.
6. P. Tabeling, *Lab Chip,* 2009, **9**, 2428-2436.
7. A. B. Theberge, F. Courtois, Y. Schaerli, M. Fischlechner, C. Abell, F. Hollfelder, and W. T. Huck, *Angew. Chem., Int. Ed.,* 2010, **49**, 5846-5868.
8. M. T. Guo, A. Rotem, J. A. Heyman and D. A. Weitz, *Lab Chip*, 2012, **12**, 2146-2155.
9. H. Song, J. D. Tice and R.F. Ismagilov, *Angew. Chem.,* 2003, **115**, 792-796.
10. B. J. Hindson, K. D. Ness, D. A. Masquelier, P. Belgrader, N. J. Heredia, A. J. Makarewicz, and B. W. Colston, *Anal. Chem. (Washington, DC, U. S.)*, 2011, **83**, 8604-8610.
11. M. M. Kiss, L. Ortoleva-Donnelly, N. R. Beer, J. Warner, C. G. Bailey, B. W. Colston and J. H. Leamon, *Anal. Chem. (Washington, DC, U. S.),* 2008, **80**, 8975-8981.
12. D. Pekin, Y. Skhiri, J. C. Baret, D. Le Corre, L. Mazutis, C. B. Salem and V. Taly, *Lab Chip*, 2011, **11**, 2156-2166.
13. Q. Zhong, S. Bhattacharya, S. Kotsopoulos, J. Olson, V. Taly, A. D. Griffiths and J. W. Larson, *Lab Chip*, 2011 , **11**, 2167-2174.
14. J. U. Shim, R. T. Ranasinghe, C. A. Smith, S. M. Ibrahim, F. Hollfelder, W. T. Huck and C. Abell, *ACS nano*, 2013, **7**, 5955-5964.
15. K. Martin, T. Henkel, V. Baier, A. Grodrian, T. Schön, M. Roth and J. Metze, *Lab Chip*, 2003, **3**, 202-207.
16. J. Clausell-Tormos, D. Lieber, J. C. Baret, A. El-Harrak, O. J. Miller, L. Frenz, C. A. Merten, *Chem. Biol. (Oxford, U. K.),* 2008, **15**, 427-437.
17. L. Frenz, A. El Harrak, M. Pauly, S. Bégin-Colin, A. D. Griffiths and J. C. Baret, *Angew. Chem., Int. Ed.,* 2008, **47**, 6817-6820.
18. H. Song, M. R. Bringer, J. D. Tice, C. J. Gerdts and R. F. Ismagilov, *Appl. Phys. Lett.*, 2003, **83**, 4664-4666.
19. D. R. Link, S. L. Anna, D. A. Weitz and H. A. Stone, *Phys. Rev. Lett.,* 2004, **92**, 054503.
20. M. C. Jullien, M. J. T. M. Ching, C. Cohen, L. Menetrier and P. Tabeling, P, *Phys. Fluids (1994-present)*, 2009, **21**, 072001.
21. K. Ahn, J. Agresti, H. Chong, M. Marquez and D. A. Weitz, *Appl. Phys. Lett.*, 2006, **88**, 264105.
22. C. N. Baroud, M. R. de Saint Vincent and J. P. Delville, *Lab Chip*, 2007, **7**, 1029-1033.
23. M. Chabert, K. D. Dorfman and J. L. Viovy, *Electrophoresis*, 2005, **26**, 3706-3715.
24. L. Mazutis, J. C. Baret and A. D. Griffiths, *Lab Chip*, 2009, **9**, 2665-2672.
25. L. Mazutis and A. D. Griffiths, *Lab Chip*, 2012, **12**, 1800-1806.
26. A. R. Abate, T. Hung, P. Mary, J. J. Agresti and D. A. Weitz, *Proc. Natl. Acad. Sci.*, 2010, **107**, 19163-19166.
27. H. Song and R. F. Ismagilov, *J. Am. Chem. Soc.*, 2003, **125**, 14613-14619.
28. S. Köster, F. E. Angile, H. Duan, J. J. Agresti, A. Wintner, C. Schmitz and D. A. Weitz, *Lab Chip*, 2008, **8**, 1110-1115
29. L. Frenz, K. Blank, E. Brouzes and A. D. Griffiths, *Lab Chip*, 2009, **9**, 1344-1348.
30. K. Ahn, C. Kerbage, T. P. Hunt, R. M. Westervelt, D. R. Link and D. A. Weitz, *Appl. Phys. Lett.*, 2006, **88**, 024104-024104.
31. J. C. Baret, O. J. Miller, V. Taly, M. Ryckelynck, A. El-Harrak, L. Frenz and A. D. Griffiths, *Lab Chip*, 2009, **9**, 1850-1858.
32. T. Franke, A. R. Abate, D. A. Weitz and A. Wixforth, A, *Lab Chip*, 2009, **9**, 2625-2627.
33. L. Mazutis, J. C. Baret, P. Treacy, Y. Skhiri, A. Fallah-Araghi, M. Ryckelynck and A. D. Griffiths, *Lab Chip*, 2009, **9**, 2902-2908.
34. A. Fallah-Araghi, J. C. Baret, M. Ryckelynck and A. D. Griffiths, *Lab Chip*, 2012, **12**, 882-891.
35. M. Seo, Z. Nie, S. Xu, M. Mok, P. C. Lewis, R. Graham and E. Kumacheva, *Langmuir*, 2005, **21**, 11614-11622.
36. Y. Song, J. Hormes and C. S. Kumar, *Small*, 2008, **4**, 698-711.
37. O. J. Miller, A. El Harrak, T. Mangeat, J. C. Baret, L. Frenz, B. El Debs and A. D. Griffiths, *Proc. Natl. Acad. Sci.*, 2012, **109**, 378-383.
38. B. El Debs, R. Utharala, I. V. Balyasnikova, A. D. Griffiths and C. A.Merten, *Proc. Natl. Acad. Sci*., 2012, **109**, 11570-11575.
39. L. Mazutis, J. Gilbert, W. L. Ung, D. A. Weitz, A. D. Griffiths and J. A. Heyman, *Nat. Protoc.*, 2013, **8**, 870-891.
40. B. Kintses, C. Hein, M. F. Mohamed, M. Fischlechner, F. Courtois, C. Lainé and F. Hollfelder, *Chem. Biol. (Oxford, U. K.)*, 2012, **19**, 1001-1009.
41. J. J. Agresti, E. Antipov, A. R. Abate, K. Ahn, A. C. Rowat, J. C. Baret and D. A. Weitz, *Proc. Natl. Acad. Sci.*, 2010, **107**, 4004-4009.
42. S. L. Sjostrom, Y. Bai, M. Huang, Z. Liu, J. Nielsen, H. N. Joensson and H. A. Svahn, *Lab Chip*, 2014, **14**, 806-813.
43. R. Tewhey, J. B. Warner, M. Nakano, B. Libby, M. Medkova, P. H. David and K. A. Frazer, *Nat. Biotechnol*, 2009, **27**, 1025-1031.
44. V. Taly, D. Pekin, L. Benhaim, S. K. Kotsopoulos, D. Le Corre, X. Li and P. Laurent-Puig, *Clin.*

Chem. (Washington, DC, U. S.), 2013, **59**, 1722-1731.

45. O. Couture, M. Faivre, N. Pannacci, A. Babataheri, V. Servois, P. Tabeling and M. Tanter, *Medical physics,* 2011, **38**, 1116-1123.
46. R. Arayanarakool, L. Shui, S. W. Kengen, A. van den Berg and J. C. Eijkel, J. C, *Lab Chip*, 2013, **13**, 1955-1962.
47. Y. Rondelez, G. Tresset, K. V. Tabata, H. Arata, H. Fujita, S. Takeuchi and H. Noji, *Nat. biotechnol.*, 2005, **23**, 361-365.
48. B. Shen, J. Ricouvier, F. Malloggi, P. Tabeling, Science, submitted.
49. I. Kobayashi, S. Mukataka and M. Nakajima, *Ind. Eng. Chem. Res.*, 2005, **44**, 5852-5856.
50. F. Malloggi, N. Pannacci, R. Attia, F. Monti, P. Mary, H. Willaime and P. Poncet, P, *Langmuir*, 2009, **26**, 2369-2373.
51. C. Cohen, R. Giles, V. Sergeyeva, N. Mittal, P. Tabeling, D. Zerrouki and N. Bremond, *Microfluid. Nanofluid.*, 1-8.
52. R. M. Lorenz, J. S. Edgar, G. D. Jeffries, Y. Zhao, D. McGloin and D. T. Chiu, *Anal. Chem. (Washington, DC, U. S.)*, 2007, **79**, 224-228.
53. R. M. Lorenz, J. S. Edgar, G. D. Jeffries, D. McGloin and D. T. Chiu, *Anal. Chem. (Washington, DC, U. S.)*, 2006, **78**, 6433-6439.
54. H. A. Pohl, *J. Appl. Phys.*, 1958, **29**, 1182-1188.
55. A. R. Thiam, N. Bremond and J. Bibette, *Phys. Rev. Lett.*, 2009, **102**, 188304.
56. N. Bremond, A. R. Thiam and J. Bibette, *Phys. Rev. Lett.*, 2008, **100**, 024501.
57. A. J. de Mello, *Lab Chip*, 2001, **1**, 24N-29N.
58. D. C. Duffy, J. C. McDonald, O. J. Schueller and G. M. Whitesides, *Anal. Chem. (Washington, DC, U. S.)*, 1998, **70**, 4974-4984.
59. P. Tabeling, P. (2010). *Introduction to microfluidics*. Oxford University Press, 2010.
60. T. W. Odom, J. C. Love, D. B. Wolfe, K. E. Paul and G. M. Whitesides, *Langmuir*, 2002, **18**, 5314-5320.
61. H. Shafiee, J. L. Caldwell, M. B. Sano and R. V. Davalos, *Biomed. Microdevices*, 2009, **11**, 997-1006.
62. A. Sciambi and A. R. Abate, *Lab Chip*, 2014
63. C. Holtze, A. C. Rowat, J. J. Agresti, J. B. Hutchison, F. E. Angile, C. H. J. Schmitz and D. A. Weitz, *Lab Chip*, 2008, **8**, 1632-1639.
64. C. Priest, S. Herminghaus and R. Seemann, *Appl. Phys. Lett.*, 2006, **88**, 024106
65. Lide, David R., [ed.]. *CRC Handbook of Chemistry and Physics.* Internet Version : s.n., 2005
66. C. N. Baroud, F. Gallaire and R. Dangla, *Lab Chip*, 2010, **10**, 2032-2045.
67. J. D. Sherwood, *J. Fluid Mech.*, 1988, **188**, 133-146.
68. V. Labrot, M. Schindler, P. Guillot, A. Colin and M. Joanicot, *Biomicrofluidics*, 2009, **3**, 012804.
69. M. H. Davis, *The Quarterly Journal of Mechanics and Applied Mathematics*, 1964, **17**, 499-511.
70. G. I. Taylor, *Proc. R. Soc. London, Ser. A*, 1964, **280**, 383-397.
71. L. Lundgaard, G. Berg, S. Ingebrigsten, P. Atten, in *Emulsions and emulsion stability*, ed. CRC Press, Boca Raton, 2nd edn., 2006, vol 132, ch. Electrocoalescence for oil-water separation.
72. J. C. Bird, W. D. Ristenpart, A. Belmonte and H. A. Stone, *Phys. Rev. Lett.*, 2009, **103**, 164502.
73. W. D. Ristenpart, J. C. Bird, A. Belmonte, F. Dollar and H. A. Stone, *Nature*, 2009, **461**, 377-380.
74. A. M. Leshansky and L. M. Pismen, *Phys. Fluids (1994-present)*, 2009, **21**, 023303.
75. P. S. Plesset and M. S. Epstein, *The Journal of Chemical Physics*, 1950, **18**, 1505.
76. P. B. Duncan and D. Needham, *Langmuir*, 2006, **22**, 4190-4197.
77. A. Q. Shen, D. Wang and P. T. Spicer, *Langmuir*, 2007, **23**, 12821-12826.
78. T. Wu, K. Hirata, H. Suzuki, R. Xiang, Z. Tang and T. Yomo, *Appl. Phys. Lett.*, 2012, **101**, 074108.
79. A. S. Kabal'Nov, A. V. Pertzov and E. D. Shchukin, *Colloids surf.*, 1987, **24**, 19-32.
80. J. Sambrook, E. F. Fritsch and T. Maniatis, in *Molecular Cloning: A Laboratory Manual,* ColdSpring Harbor Laboratory Press, Plainview, N. Y., 2nd edn., 1989